

Design Methodology and Experimental Verification of Serpentine/Folded-Waveguide TWTs

Khanh T. Nguyen, *Member, IEEE*, Alexander N. Vlasov, *Senior Member, IEEE*,
 Lars Ludeking, Colin D. Joye, *Senior Member, IEEE*, Alan M. Cook, *Member, IEEE*,
 Jeffrey P. Calame, *Senior Member, IEEE*, John A. Pasour, *Senior Member, IEEE*,
 Dean E. Pershing, Edward L. Wright, Simon J. Cooke, *Senior Member, IEEE*,
 Baruch Levush, *Fellow, IEEE*, David K. Abe, *Senior Member, IEEE*,
 David P. Chernin, and Igor A. Chernyavskiy, *Member, IEEE*

Abstract—The general electromagnetic properties and design methodology for serpentine/folded-waveguide (FW) amplifiers are presented. In addition, hybrid-waveguide circuit topologies, which permit greater design flexibility than the basic serpentine/FW topologies, are also introduced, and their dispersion characteristics are discussed. Experimental validation of design methodology and tools is provided via test results of the recently demonstrated wideband 220-GHz serpentine amplifier, which embodies the design methodology described herein. Particular attention will be paid to the comparison between code prediction and experimental data, which are in excellent agreement.

Index Terms—Amplifier, backward-wave oscillation (BWO), dispersion, folded waveguide (FW), oscillation, serpentine, stopband, traveling-wave tube (TWT), vacuum electronics.

I. INTRODUCTION

DEVELOPMENT of high-power broadband vacuum electron devices (VEDs) beyond Ka-band using conventional coupled-cavity and helix traveling-wave tube (TWT) RF circuit fabrication techniques is challenging due to uncertainties in the fabrication and assembly of these small RF circuits. Serpentine and folded-waveguide (FW) TWTs are a class of VEDs capable of wideband high-power performance and prove less sensitive to fabrication uncertainties. The unique advantage of these devices resides in their structural simplicity;

Manuscript received December 6, 2013; accepted January 6, 2014. Date of publication April 23, 2014; date of current version May 16, 2014. This work was supported by the U.S. Office of Naval Research. The review of this paper was arranged by Editor W. L. Menninger.

K. T. Nguyen, D. E. Pershing, and E. L. Wright are with Beam Wave Research Inc., Bethesda, MD 20814 USA (e-mail: knguyen.bwresearch@comcast.net; dean.pershing@nrl.navy.mil; ewright.bwresearch@comcast.net).

A. N. Vlasov, C. D. Joye, A. M. Cook, J. P. Calame, J. A. Pasour, S. J. Cooke, B. Levush, D. K. Abe, and I. A. Chernyavskiy are with the Naval Research Laboratory, Washington, DC 20375 USA (e-mail: Alexander.vlasov@nrl.navy.mil; colin.joye@nrl.navy.mil; alan.cook@nrl.navy.mil; jeffrey.calame@nrl.navy.mil; john.pasour@nrl.navy.mil; ewright.bwresearch@comcast.net; baruch.levush@nrl.navy.mil; dave.abe@nrl.navy.mil; igor.chernyavskiy@nrl.navy.mil).

L. Ludeking is with ATK/Mission Research, Newington, VA 22122 USA (e-mail: lars.ludeking@atk.com).

D. P. Chernin is with Leidos Inc., Washington, DC 20375 USA (e-mail: david.chernin@saic.com).

Color versions of one or more of the figures in this paper are available online at <http://ieeexplore.ieee.org>.

Digital Object Identifier 10.1109/TED.2014.2303711

circuit geometry prior to introducing the beam tunnel is a fixed-profile extrusion. Therefore, these devices and their properties have been the focus of intense research and development for millimeter and submillimeter regimes [1]–[12], where various monolithic microfabrication techniques are employed for RF circuit fabrication.

The promise of these devices was first realized in [3] with the demonstration of several *Q*-band two-stage serpentine TWTs that produced 135 W of average power and saturated gains of ~ 30 dB over an impressive 25% instantaneous bandwidth. More recently, with the advances in microfabrication approaches, a number of serpentine TWTs with progressively higher frequencies have been successfully realized. These include: a 110-W 94-GHz TWT developed by L3-Electron Devices Division [9], a 63-W G-band TWT at the Naval Research Laboratory (NRL) [10], and a 110-mW 670-GHz TWT demonstrated by Northrop-Grumman [11]. The successful demonstration of these devices serves as proof that this class of VEDs represents a key pathway toward the development of future advanced amplifiers in the millimeter and submillimeter regimes. Thus, serpentine and FW TWTs have been a focus of research and development at the Naval Research Laboratory.

In this paper, we describe our design methodology, its application to amplifier designs, and our experience of its utility in practice. For TWTs, synchronism between the RF fields and the electron beam is the key to beam-wave interaction. This will be the focus of Section II, where the basic serpentine waveguide dispersion and its relationship to the electron beam line are presented. Impact of the beam tunnel and various fabrication imperfections on the dispersion are also discussed. Properties of serpentine and FW are also compared in this section. A new type of circuit, the hybrid waveguide, is introduced as part of this discussion. Backward-wave oscillation (BWO) and mitigation approaches for these circuit types are also presented in this section.

Section III presents the design of the recently demonstrated G-band TWT amplifier [10], which employs the design methodology described in Section II. This device was originally intended as an experimental validation of design methodology and tools and also as a microfabrication

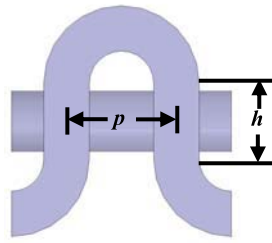


Fig. 1. Basic element of a serpentine circuit with beam tunnel. p is the period or interaction gap-gap distance and h is the length of the straight vertical segment. The width of waveguide measured in the page is a .

demonstration. Thus, particular attention will be paid to the comparison between code prediction and experimental data, which are in excellent agreement. This is a critical step in ensuring confidence in the design of future amplifiers. Section IV summarizes our results.

II. CIRCUIT CHARACTERISTICS

The basic serpentine circuit can be easily understood as a simple TE₁₀ waveguide bent into the shape of a serpent to slow down the speed of the RF power flow into approximate synchronism with the electron beam, and more importantly, to align the transverse component of the waveguide RF electric field with the electron beam direction at the interaction gaps. Fig. 1 shows the basic element of the serpentine circuit including the beam tunnel.

A. Dispersion

For a waveguide of width a for which the TE₁₀ angular cutoff frequency is $\omega_c = \pi c/a$ (c is the speed of light), the dispersion can simply be expressed as

$$\omega^2 = \omega_c^2 + k_s^2 c^2 \quad (1)$$

where ω and k_s are the angular frequency and the wavenumber along the curvilinear serpentine waveguide axis, respectively. As written, (1) is identical to that of a straight waveguide, and the relative phase shift between the two positions is simply k_s times the relative distance along the waveguide axis. However, from the beam-wave interaction standpoint, the key phase shift is the phase shift from gap-to-gap as observed by the electron beam. This phase shift ϕ_z can be related to the waveguide's wavenumber k_s through

$$\phi_z = k_s L + \pi. \quad (2)$$

Here, $L = h + \pi p/2$ is simply the path length along a half-period of the serpentine waveguide (i.e., from gap to gap), which includes the bend, $\pi p/2$. As shown in Fig. 1, p is the axial spacing between the gaps, and h is the vertical length of the straight segment. The extra π phase shift in (2) is due to the effect of the bend, which reverses the orientation of the RF electric field as observed along the beam direction.

Equations (1) and (2) together give us the dispersion relation for the serpentine waveguide circuit. This can be written in a

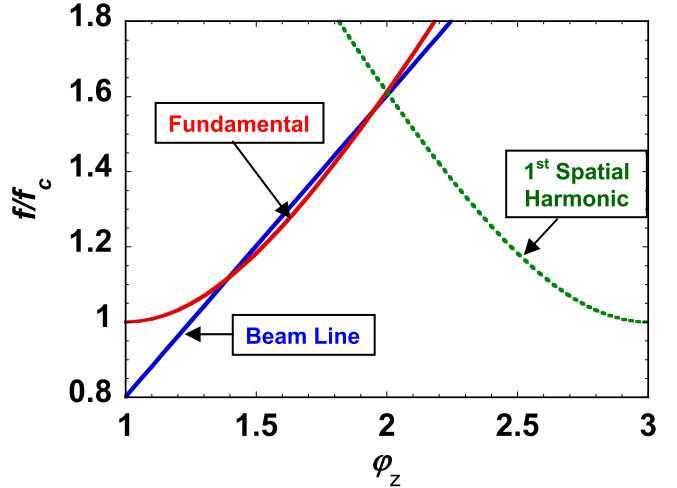


Fig. 2. Illustration of serpentine circuit dispersion with beam line. Phase shift is normalized by π .

simplified normalized form as

$$(f/f_c)^2 = 1 + \frac{a^2}{L^2} \left[\frac{\phi_z}{\pi} - (2n + 1) \right]^2. \quad (3)$$

In (3), f and $f_c = c/(2a)$ are the RF and TE₁₀ cutoff frequencies, respectively. The integer $n (= \pm 1, \pm 2, \pm 3 \dots)$ denotes the spatial harmonics due to the inherent periodic nature of the circuit with $n = 0$ being the fundamental component. This dispersion is similar to the dispersion relationships used for FW TWTs design in the pioneer work of Dohler *et al.* [2] and later in [4] and [5].

As for the electron beam, its modulation frequency f_b can also be related to the gap-to-gap phase shift ϕ_z through its axial velocity v_z via the relation $f_b = (v_z/p)(\phi_z/2\pi)$. This relation can be written in normalized form as

$$f_b/f_c = \frac{a}{p} \beta_e \phi_z. \quad (4)$$

Here, $\beta_e = v_z/c$. Shown in Fig. 2 is an example of a serpentine TWT dispersion and the associated electron beam line for wideband application. To first order, the bandwidth of serpentine TWTs is limited at the lower end by the waveguide cutoff frequency, f_c , and at the higher end at the intersection of the forward-wave component of the fundamental ($n = 0$) waveguide mode with the backward-wave component of the first spatial harmonic ($n = 1$), $f_{2\pi}$, which are given by

$$(f_{2\pi}/f_c)^2 = 1 + \frac{a^2}{L^2}. \quad (5)$$

B. Impact of Beam Tunnel

The dispersion shown in Fig. 2 is that for an ideal serpentine circuit without the effect of the bends or beam tunnel. It should be noted that the bends do introduce a small stopband at the 2π point [given by (5)] even without the beam tunnel. However, the presence of the beam tunnel can further exacerbate the perturbation and introduce a substantial stopband. The larger the beam tunnel radius, the larger the stopband that results.

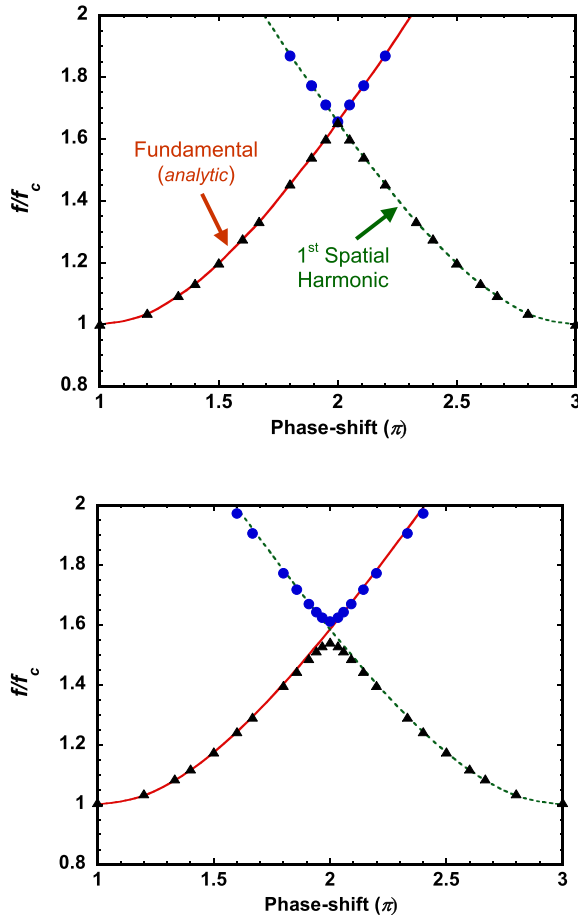


Fig. 3. Simulated dispersion (symbols) versus analytic dispersion (lines) for two values of α , 0.115 (top) and 0.192 (bottom). Note the stopband in the bottom plot.

In general, the simple metric for determining the impact is the ratio of the beam tunnel size to the free-space wavelength of the 2π frequency. This can be expressed by the parameter α defined as

$$\alpha = \frac{R_T}{L} \times \left(1 + \frac{L^2}{a^2}\right)^{1/2}. \quad (6)$$

R_T is the beam tunnel radius, which, of course, is determined primarily by beam optics and transport considerations. We have empirically found via 3-D electromagnetic simulations that the approximate threshold for a stopband is $\alpha \approx 0.115$, above which the stopband is observable. The impact of α is shown in Fig. 3, where the simulated dispersions are shown for two values of α , 0.115 and 0.192. Also shown in the figure are the analytical dispersion curves as given by (3). Excellent agreement with the simulated data can clearly be observed.

As observed in the figure, the stopband for small beam tunnel ($\alpha = 0.115$) is virtually nonexistent, whereas, in the larger beam tunnel case ($\alpha = 0.192$), a readily observable stopband has developed. The primary physical reason for this stopband is similar to that of a waveguide with periodic perturbation, e.g., a disk loaded waveguide. As the frequency approaches the point where the corresponding half axial wavelength is equal to the spacing between the perturbations, reflections add up in phase creating resonances (standing waves), and the RF power

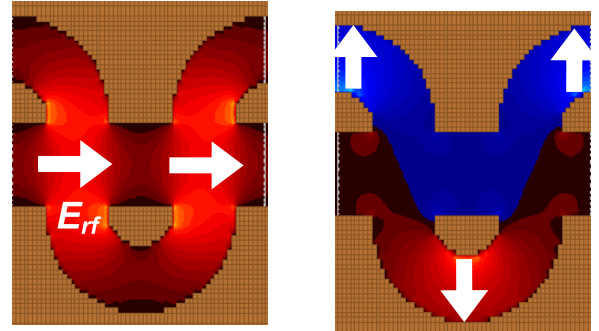


Fig. 4. MAGIC simulated 2π eigenmodes for upper (left) and lower (right) passbands for the larger beam tunnel case shown in Fig. 3.

can no longer propagate, hence the stopband. Obviously, larger perturbations will result in a larger stopband. For straight waveguide, the stopband is at the π point, but it will be at the 2π point for serpentine waveguide due to the extra π phase shift introduced by the bends.

It is instructive to examine the mode patterns at the 2π point as they have important implications on beam-wave interactions. These are shown in Fig. 4, which illustrates the 2π eigenmodes for both the upper and lower pass bands as simulated by MAGIC-3-D. The results shown here correspond to the larger beam tunnel case shown in the bottom plot of Fig. 3.

It can be observed that there exists a strong RF axial field component along the beam axis near the 2π point in the upper passband and minimal RF field in the lower passband. From a beam-wave interaction standpoint, this implies that BWOs can be excited if the beam line intersects the upper passband near this point but are unlikely in the lower passband. This serpentine circuit is also less likely to exhibit drive-induced oscillations than coupled-cavity TWTs [13], as the interaction impedance is weak in the lower passband near the 2π point while the dispersion curve is more sharply peaked than that of typical coupled-cavity circuits (which limits the range of phases over which the group velocity is low).

A serpentine circuit BWO excitation is shown in Fig. 5. As shown in the top plot, the beam line intersects with the upper passband just before the 2π phase-shift point, a condition optimal for BWO. The spontaneous excitation as modeled by MAGIC-3-D [14] is illustrated by the middle and bottom plots, which show beam trajectories in the circuit and the backward RF power flow, respectively. Such excitation can be avoided by ensuring the beam line frequency at the 2π point is just below that of the upper passband at the nominal operation parameters. This was the approach taken in our G-band TWT design to be described in Section III. However, if design requirements necessitate such an intersection between the beam line and the upper passband, it is important that the length of each individual stage in the TWT be kept below the critical length for such spontaneous excitation, as is the case in our W-band design [15].

C. FW and Hybrid-Waveguide Circuits

The basic FW slow-wave circuit is similar to the basic serpentine circuit, in that, a simple TE_{10} waveguide is sharply

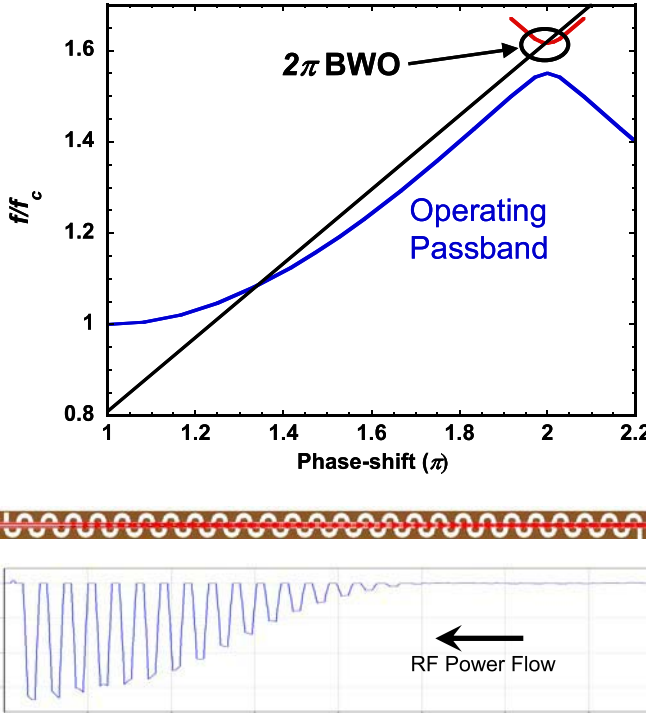


Fig. 5. RF dispersion and beam line conducive to BWO (top). Beam trajectories (middle) and RF power flow (bottom) from a corresponding MAGIC simulation.

folded to slow down the speed of the RF power flow. Thus, it exhibits the same behavior as that for the serpentine circuit, and basic dispersion expressions, such as (3), still apply. In this case, the path length from gap-to-gap is given by $L = h + b + p$, where h is as defined in the top left plot of Fig. 6 is the vertical distance between the inner edges of the folds, b is the waveguide narrow guide dimension, and p is still the axial gap-gap spacing. In fact, when both serpentine and FW circuits have the same dispersion, particle-in-cell (PIC) simulations indicates that beam–wave interactions are also the same. This has been demonstrated via simulations of our three-beam cascaded TWT design [16].

In both the basic serpentine and FW circuit, b stays constant throughout the circuit and is dictated primarily by the beam transit angle for optimal beam–wave coupling. This, together with the stopband potentially introduced by the beam tunnel, limits the design flexibility, which compromises the potential for optimal amplifier performance. An extra degree of freedom in the circuit topology would be both desirable and necessary to achieve optimal beam–wave coupling and tailor the dispersion near the 2π point to avoid BWO. This is indeed feasible via the hybrid-waveguide circuits shown by the top right and bottom plots in Fig. 6 for both the FW and serpentine configurations, respectively. By allowing the narrow guide dimension to be different in the folds than in the bends, one gains an additional degree of freedom that can be used to widen the stopband or remove it all together.

To demonstrate the utility of the extra hybrid circuit dimension, we consider the FW circuit shown in the top right plot of Fig. 6. Here, b is the narrow dimension in the vertical section (interaction gap) and b_f is the narrow dimension of the folds.

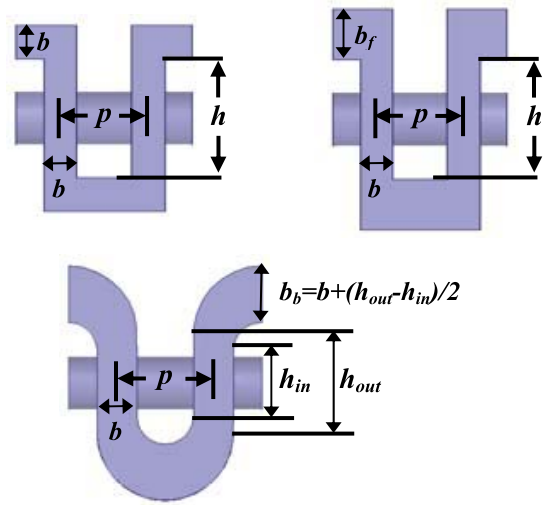


Fig. 6. Schematic views of a basic FW (top left), a hybrid FW (top right), and a hybrid serpentine (bottom) circuit.

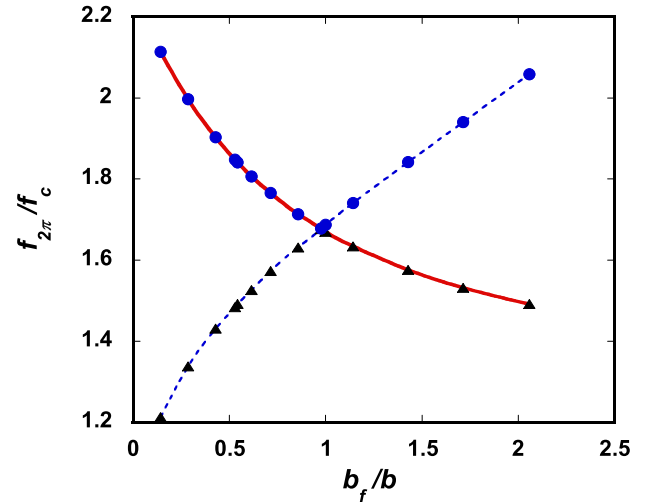


Fig. 7. Calculated dependence of 2π frequencies of upper (●) and lower (▲) passbands on b_f/b . Solid (dashed) lines represent points with nonzero (zero) RF field on axis.

Thus, the gap-to-gap RF path length is $L = h + b_f + p$. The dispersive properties of this hybrid circuit are computed with the 3-D electromagnetic code ANALYST [17]. In the parametric study shown in Fig. 7, we keep p , b , and beam tunnel radius constant. Only h and b_f are varied in such a way that the RF gap-to-gap path length L is kept constant. The 2π frequencies of the upper (circles) and lower (triangles) passbands are plotted as a function of b_f/b . In this particular example, the passbands coalesce (no stopband) near unity, as we have chosen to keep the beam tunnel size to be below the threshold given in (6). Irrespective of beam tunnel sizes, with this new topology, a circuit designer essentially has the flexibility to widen the stopband or to coalesce the passbands by selecting the proper ratio of b_f/b depending on the need and subject to geometrical constraints. Variations of the b_f/b ratio in both directions from the coalescent modes point will lead to opening of the stopband.

Another important factor to note is the beam tunnel on-axis interaction impedance as was discussed in [18] and first identified in [7]. This effect is shown in Fig. 7 by the solid line, which connects the 2π frequency points with nonzero axial RF field on the axis of the beam tunnel [similar to the example shown in Fig. 4 (left)]. In contrast, the dashed line indicates points with zero axial electric field on the axis. As can be observed in the figure, the strong on-axis axial RF field interchanges between the upper and lower passbands at the point of coalescence. Obviously, modes with nonzero axial RF field are more dangerous in terms of parasitic mode excitation. Thus, particular attention must be paid to not only the stopband itself but also to the properties of the interaction impedance at the band edges.

Similar behavior can also be achieved with the hybrid serpentine circuit topology shown in the bottom plot of Fig. 6 with critical dimensions defined. Therein, the vertical distances between the upper and lower centers of bend curvature for both the inner and outer bends are defined as h_{in} and h_{out} , respectively. The case shown in Fig. 6 is when $h_{out} > h_{in}$. As in the hybrid FW topology, the basic serpentine is also simply a special case of this topology, where $h_{in} = h_{out}$. The distance between the inner and outer bends at the bend apex, defined as b_b in the figure, is given by $b_b = b + (h_{out} - h_{in})/2$, which serves the same function as b_f in the hybrid FW topology. The gap-to-gap RF path length is simply $L = \pi p/2 + (h_{out} + h_{in})/2$. Thus, b_b and L can be independently controlled via the difference and mean of h_{in} and h_{out} , respectively.

D. Circuit Imperfections

Thus far, the discussion has focused on ideal circuits. However, imperfections due to fabrication errors can introduce a spurious stopband, which has an adverse impact on amplifier performance. The most obvious of these is caused by beam tunnel offset in the E-plane, where the beam tunnel is no longer symmetric relative to the top and bottom bends of a serpentine circuit. Referring back to the straight waveguide case, this is equivalent to having biperiodic perturbations, which would impact the stopband near the π point (near since this point is no longer singularly defined). Moreover, biperiodicity will also result in formation of a new stopband near the $3\pi/2$ point. The latter point is due to reflections created when the axial wavelength is equal to the combined periods of the biperiodic perturbations. In serpentine/FW circuit, the impact of biperiodicity is observed near the $3\pi/2$ due to the extra π phase shift.

Issues associated with beam tunnel offset/tilt are most pronounced for high-frequency devices, such as our wideband 220-GHz TWT, due to the small characteristic length scale of such devices, hence the challenge in beam tunnel alignment. We refer the reader to [10] for a detailed experimental illustration of the impact of such beam offset/tilt. For a wideband amplifier, the high reflection at the $3\pi/2$ frequency within the operating band can cause a gain dip or, worse, oscillation at this frequency.

It is important to note that the stopband at $3\pi/2$ is not necessarily only caused by beam tunnel offset/tilt. Biperiodicity can

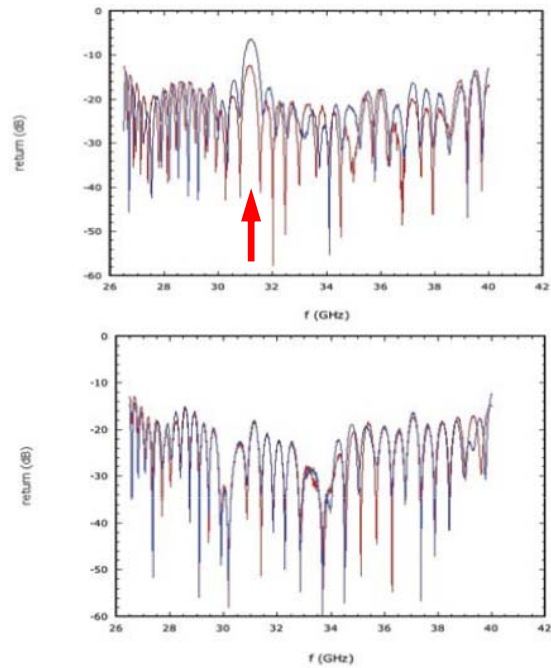
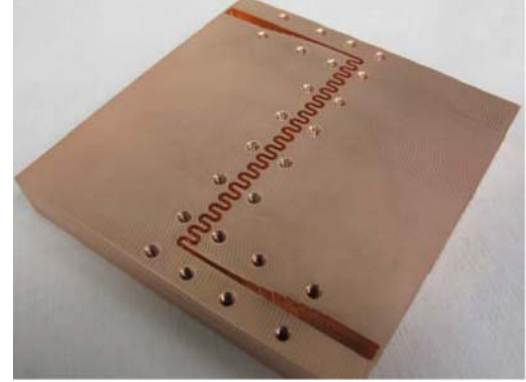


Fig. 8. S_{11} (dB) versus frequency cold-test circuits: early tests without beam tunnel (top, with $3\pi/2$ mode marked with arrow) and later results with beam tunnel (bottom).

be introduced also by difference of the top and bottom bends of FW. Recent Ka-band serpentine circuit fabrication tests with Computer Numerical Control milling at the NRL demonstrated that such stopband can be created by very small difference (hardly noticeable via metrology) in the top and bottom bends introduced by the fabrication process. Fig. 8 (top) shows one such test circuit. The measured reflection (S_{11}) for two early test circuits is shown in Fig. 8 (middle). A strong reflection can be observed at the $3\pi/2$ frequency as marked by the arrow. This response is quite consistent, and most remarkably, these circuits do not even have a beam tunnel. This clearly indicates systematic errors in the serpentine circuit fabrication process. With careful analysis and slight modification in the fabrication sequence, this issue has now been resolved. This is illustrated by cold-test data shown in Fig. 8 (bottom) for two recently fabricated circuits. These newer circuits also incorporate beam tunnels, indicating good tunnel alignment with the serpentine circuit. Furthermore, fabrication repeatability is also indicated

by the similarity between the responses of the two separate circuits shown in the bottom plot.

III. G-BAND CIRCUIT DESIGN AND EXPERIMENTAL VALIDATION

The primary motivation for the G-band amplifier was to develop a high-power broadband serpentine TWT amplifier, which would serve as an experimental validation of design methodology and tools and also as a microfabrication technology demonstration. To expedite the amplifier development process and to mitigate development risks, it was decided *a priori* that circuit design must conform to the existing beamstick (gun, magnet, and collector) developed by Communications and Power Industries (CPI/Canada) for the NRL for use in a 5-W continuous-wave 218-GHz extended-interaction klystron (EIK) amplifier (Model VKY-2444T). This beam stick yields a nominal electron beam of 117 mA at 11.7 kV, which is focused by an intense solenoidal magnetic field.

The circuit design was performed with MAGIC-3-D using electron beam phase space data imported from MICHELLE simulations of the existing electron gun. To avoid BWO, the electron beam line is placed just slightly below the 2π frequency of the upper passband of the circuit dispersion at the nominal operating voltage. The final design employed a 64-gap single-stage circuit configuration, which was the limit imposed by spatial constraints in the existing beamstick. At nominal beam parameters, design simulations predicted a small signal circuit gain of approximately 18 dB and a saturated output power of 63 W. This design formed the basis for the circuit microfabrication effort via UV-LIGA described in detail in [19]. In addition, this design was used for benchmarking purposes for two newly developed tools at NRL, the 3-D PIC code Neptune [20] and 2-D large-signal design code TESLA-FW [21].

Upon the completion of the circuit fabrication and cold test at NRL, the circuit was integrated with the beam stick by CPI/Canada, and the completed amplifier was delivered to NRL for performance test. Shown in Fig. 9 is the completed amplifier under test at NRL. Also shown in the figure are the design circuit dispersion and the beam line at nominal operating voltage of 11.7 kV. The reasons for the relative placement of the beam line and circuit dispersion shown are threefold: 1) to ensure the amplifier is stable against BWO; 2) to effect wideband operation; and 3) to permit the contingency of voltage tuning, if necessary, for compensating potential deleterious effects due to any small fabrication errors. The last of these was a major concern prior to full amplifier demonstration.

Under tests, the amplifier performed as intended and was zero drive stable at the nominal operating parameters. Fig. 10 shows comparisons of small-signal gain curves versus frequency between measured data (dashed lines with symbols) and early simulations with MAGIC-3-D (solid lines) for several beam test voltages. Gain ripples observed in the test data can partly be attributed to reflections from brazed joints in the input and output waveguides [10]. These mismatches were not modeled in the simulations, which use as-designed

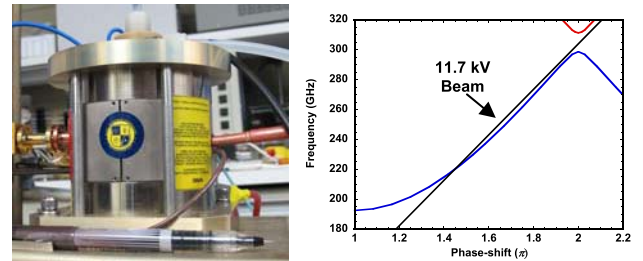


Fig. 9. G-band amplifier under test at NRL (left) and design circuit dispersion with beam line at nominal beam voltage of 11.7 kV (right).

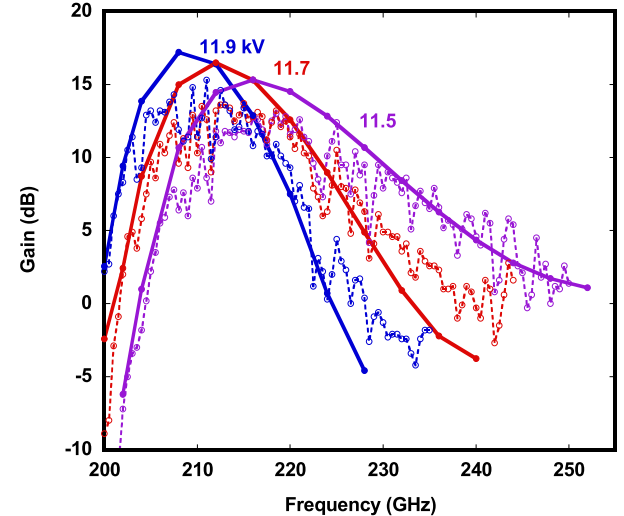


Fig. 10. Small-signal frequency response comparisons between MAGIC predictions (solid) and test data (dashed with symbols) for three beam voltages.

circuit dimensions. However, the simulations include two known nonideal factors, which were identified prior to circuit integration into the amplifier. The first of these is a small beam tunnel offset relative to the circuit bends, and the second is the slightly smaller than designed beam tunnel diameter. The transmitted beam current in these cases is approximately 103 mA, which was also used in the simulations. This beam current is lower than the nominal design value of 117 mA and can be attributed partly to the smaller as-built beam tunnel. Consequently, the actual circuit gain is reduced by approximately 3 dB relative to the design gain. As can be observed from the figure, the good correlation between the simulated and measured data indicates the as-built circuit dimensions conformed quite closely to the as-designed dimensions. This is a remarkable achievement considering the small circuit dimensions in this frequency regime and the novel circuit microfabrication approach being employed for the first time here.

As noted earlier, an integral part of this effort was also to validate new and computationally efficient design tools, one of which is the newly developed 3-D PIC code Neptune [20]. This is a graphical processing unit-based code, which improves computational throughput by orders of magnitude relative to MAGIC. In addition, Neptune incorporates a new cut-cell approach that more accurately represents curved surfaces,

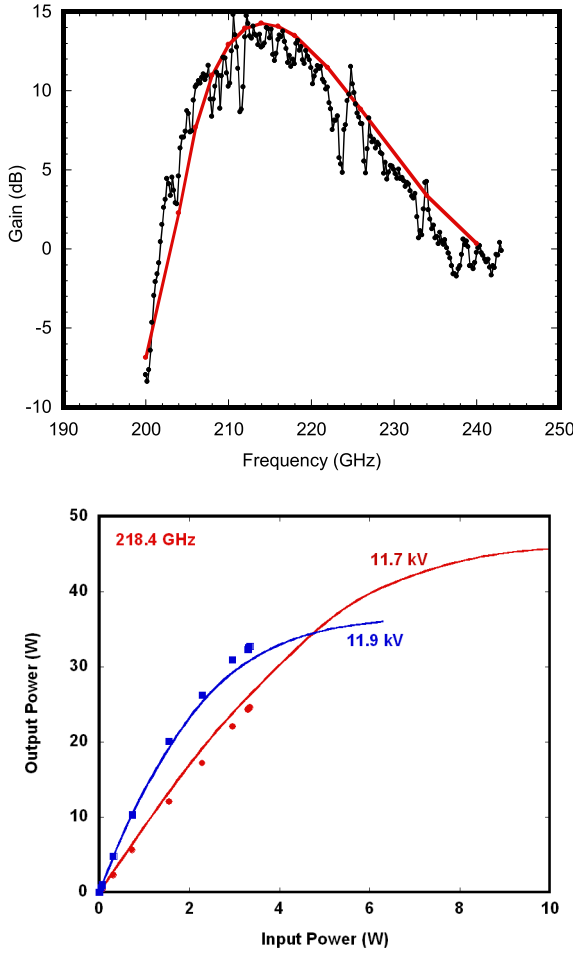


Fig. 11. Comparisons between Neptune predictions and test data on small signal frequency response at 11.7 kV (top) and transfer curves at 218.4 GHz for beam voltages of 11.7 and 11.9 kV, where test data are shown as symbols (bottom).

such as the bends in serpentine circuits. Thus, subsequently, Neptune was primarily used to model the observed experimental data. Shown in Fig. 11 are the comparisons between Neptune modeling results and experimental data for the small-signal frequency response at the nominal operating voltage of 11.7 kV (top) and also the transfer curves for two different voltages as achieved with available drive power from the EIK (bottom). These simulations also incorporate some slight geometrical variations from the designed geometry that were deduced from a detailed examination of the as-built circuit cold-test data, which were not available at the time the simulations shown in Fig. 10 were performed. As can be observed, the agreement between measured performance and code predictions is excellent. Further comparisons between Neptune and test data are presented in [10]. Similar agreement was also achieved with TESLA-FW [22].

The maximum saturated output power of 63 W was measured at 214.4 GHz at beam voltage of 12.1 kV. At voltages above 12.2 kV, oscillations were observed. This is also approximately the voltage range where BWO is expected as predicted by simulations.

We end this section by noting that the validation of the design methodology and tools plus the experience gained

through this exercise provide the necessary foundation for the development of future serpentine/FW amplifiers.

In fact, this validated design methodology and tools have also been utilized in the designs for two other amplifiers. The first of these amplifiers is a W-band serpentine TWT with >200 W of power over a 4-GHz bandwidth (>100 W over 7 GHz). This amplifier is driven by a 122-mA 20 kV electron beam. Predicted RF peak power is 245 W, corresponding to 10% electronic efficiency [12]. The second is a three-beam Ka-band cascaded TWT. This amplifier will be driven by an electron gun (0.6 A \times 3, 20 kV) adapted from our 18-beam multiple-beam klystron gun design [23]. Both serpentine and FW versions of the cascaded TWT have been evaluated. Peak RF power of 4.5 kW is expected at 100-W drive power at center frequency of 30 GHz with minimum output power of 3 kW over a 5-GHz (4 kW over >2 GHz) frequency band [13]. Both of these amplifiers are currently under development at NRL.

IV. CONCLUSION

In this paper, the general electromagnetic properties and design methodology for serpentine/FW amplifiers have been presented and discussed. The discussed properties include the basic serpentine/FW dispersion, its relationship to the electron beam line, and the impact of the beam tunnel and various fabrication imperfections on the dispersion. The hybrid-waveguide circuit topologies, which permit greater design flexibility than the basic serpentine/FW topologies, have also been introduced, and their properties are analyzed and contrasted. BWO and mitigation approaches for these circuit types are also presented.

We presented the design of the recently demonstrated NRL G-band TWT amplifier, which embodied the design methodology described herein. This device was originally intended as an experimental validation of design methodology and tools and also as a microfabrication demonstration. Thus, a detailed discussion was devoted to comparing and contrasting its test data against design predictions and also simulation models, which incorporated known as-built variations. As presented, test results, design predictions, and code modeling are in general excellent agreement. This agreement is important from two different standpoints. First, it indicates that the as-built circuit dimensions conformed quite closely to the as-designed dimensions, which is a validation of the novel circuit microfabrication approach being employed for the first time here. This is quite remarkable considering the small circuit dimensions in this frequency regime. Second, it also serves as an experimental validation for our design tools (MAGIC and Neptune PIC codes, large signal code TESLA-FW, gun/collector code MICHELLE, 3-D electromagnetic code ANALYST, etc.) and methodology, a critical step in the design of future amplifiers.

REFERENCES

- [1] J. L. Putz, W. R. Luebke, W. A. Harman, and K. R. Spangenberg, "Operating characteristics of a folded-line traveling-wave tube," Electron. Res. Lab., Stanford Univ., Stanford, CA, USA, Tech. Rep. 15, Jul. 1952.
- [2] G. Dohler, D. Gagne, D. Gallagher, and R. Moats, "Serpentine waveguide TWT," in *Proc. IEDM*, 1987, pp. 485–488.

- [3] G. Dohler, D. Gallagher, and J. Richards, "Millimeter wave folded waveguide TWTs," in *Proc. Vac. Electron. Ann. Rev.*, Crystal City, VA, USA, 1993, pp. V15–V20.
- [4] Y. H. Na, S. W. Chung, and J. J. Choi, "Analysis of a broadband Q band folded waveguide traveling-wave tube," *IEEE Trans. Plasma Sci.*, vol. 30, no. 3, pp. 1017–1023, Jun. 2002.
- [5] S.-T. Han, J.-I. Kim, and G.-S. Park, "Design of a folded waveguide traveling wave tube," *Microw. Opt. Technol. Lett.*, vol. 38, no. 2, pp. 161–165, 2003.
- [6] J. H. Booske, M. C. Converse, C. L. Kory, C. T. Chevalier, D. A. Gallagher, K. E. Kreischer, *et al.*, "Accurate parametric modeling of folded waveguide circuits for millimeter-wave travelling wave tubes," *IEEE Trans. Electron Device*, vol. 52, no. 5, pp. 685–694, May 2005.
- [7] R. Carter, "An improved equivalent circuit model of folded-waveguide slow-wave structures," in *Proc. Displays Vac. Electron.*, Garmisch-Partenkirchen, Germany, May 2001, pp. 55–59.
- [8] M. Basten, J. Tucek, D. Gallagher, K. Kreischer, J. Liu, L. Ives, *et al.*, "A multiple electron beam array for a 220 GHz amplifier," in *Proc. IEEE IVEC*, Monterey, CA, USA, Apr. 2009, pp. 110–111.
- [9] R. Kowalczyk, A. Zubyk, C. Meadows, M. Martin, M. Kirshner, R. True, *et al.*, "A 100 Watt W-Band MPM TWT," in *Proc. 14th IEEE IVEC*, Paris, France, May 2013, pp. 1–2.
- [10] C. D. Joye, A. M. Cook, J. P. Calame, D. K. Abe, K. T. Nguyen, E. L. Wright, *et al.*, "Demonstration of a high power, wideband 220 GHz serpentine waveguide amplifier fabricated by UV-LIGA," in *Proc. 14th IEEE IVEC*, Paris, France, May 2013, pp. 1–2.
- [11] J. C. Tucek, M. A. Basten, D. A. Gallagher, K. E. Kreischer, R. Lai, V. Radisic, *et al.*, "A 100 mW, 0.670 THz power module," in *Proc. IEEE 13th Int. Vac. Electron. Conf.*, Monterey, CA, USA, Apr. 2012, pp. 31–32.
- [12] J. C. Tucek, M. A. Basten, D. A. Gallagher, and K. E. Kreischer, "Testing of a 0.850 THz vacuum electronic power amplifier," in *Proc. IEEE 14th IVEC*, Paris, France, May 2013, pp. 1–2.
- [13] M. Cusick, R. Begum, D. Gajaria, T. Grant, P. Kolda, J. Legarra, *et al.*, "Wide band Ka-band coupled-cavity traveling wave tube (CCTWT) development," in *Proc. IEEE 13th Int. Vac. Electron. Conf.*, Monterey, CA, USA, Apr. 2012, pp. 225–226.
- [14] B. Goplen, L. Ludeking, D. Smith, and G. Warren, "User-configurable MAGIC for electromagnetic PIC calculations," *Comput. Phys. Commun.*, vol. 87, no. 1, pp. 54–86, 1995.
- [15] K. Nguyen, L. Ludeking, A. Cook, S. Cooke, C. Joye, J. Calame, *et al.*, "Design of a wideband high power W-band serpentine waveguide TWT," in *Proc. IEEE 14th Int. Vac. Electron. Conf.*, Paris, France, May 2013, pp. 1–2.
- [16] K. Nguyen, D. Pershing, J. Pasour, L. Ludeking, E. Wright, R. Myers, *et al.*, "Development of high-power broadband Ka-band cascaded-TWT," in *Proc. IEEE 14th Int. Vac. Electron. Conf.*, Paris, France, May 2013, pp. 1–2.
- [17] (2014, Feb. 14). *ANALYST 3D Electromagnetic Simulation and Analysis Software* [Online]. Available: <http://web.awrcorp.com/Usa/Products/Analyst-3D-FEM-EM-Technology/>
- [18] T. M. Antonsen, A. N. Vlasov, D. P. Chernin, I. A. Chernyavskiy, and B. Levush, "Transmission line model for folded waveguide circuits," *IEEE Trans. Electron Devices*, vol. 60, no. 9, pp. 2906–2911, Sep. 2013.
- [19] C. D. Joye, A. M. Cook, J. P. Calame, D. K. Abe, A. N. Vlasov, I. A. Chernyavskiy, *et al.*, "Microfabrication and cold testing of copper circuits for a 50-watt 220-GHz traveling wave tube," *Proc. SPIE*, vol. 8624, pp. 1–6, 2013.
- [20] S. J. Cooke, I. A. Chernyavskiy, G. M. Stanchev, B. Levush, and T. M. Antonsen, "GPU-accelerated 3D large-signal device simulation using the particle-in-cell code 'Neptune,'" in *Proc. IEEE Int. Vac. Electron. Conf.*, Monterey, CA, USA, Apr. 2012, pp. 21–22.
- [21] I. Chernyavskiy, A. N. Vlasov, B. Levush, T. M. Antonsen, and K. T. Nguyen, "Parallel 2D large-signal modeling of cascaded TWT amplifiers," in *Proc. IEEE Int. Vac. Electron. Conf.*, Paris, France, May 2013, pp. 1–2.
- [22] A. N. Vlasov, I. A. Chernyavskiy, C. D. Joye, A. M. Cook, J. P. Calame, B. Levush, *et al.*, "Modeling of the NRL G-Band serpentine waveguide TWT using CHRISTINE and TESLA simulation codes," in *Proc. IEEE Int. Vac. Electron. Conf.*, Paris, France, May 2013, pp. 1–2.
- [23] K. Nguyen, D. E. Pershing, D. K. Abe, G. Miram, and B. Levush, "Eighteen-beam gun design for high power, high repetition rate, broadband multiple-beam klystrons," *IEEE Trans. Plasma Sci.*, vol. 33, no. 2, pp. 685–695, Apr. 2005.

Authors' photographs and biographies not available at the time of publication.